Ocean Engineering 198 (2020) 106963

Contents lists available at ScienceDirect

Ocean Engineering

journal homepage: www.elsevier.com/locate/oceaneng

A novel hybrid monopile foundation for offshore wind turbines

Hongwang Ma [a,*], Jun Yang [a,b]

[a] School of Naval Architecture, Ocean and Civil Engineering, Shanghai Jiao Tong University, Shanghai, China
[b] Department of Civil Engineering, The University of Hong Kong, Hong Kong, China

ARTICLE INFO

Keywords:
Offshore wind turbine
Monopile
Concrete-filled double skin steel tubular structure
Accumulated rotation
Natural frequency

ABSTRACT

This paper presents a hybrid monopile foundation for offshore wind turbines. It is an ultra-high performance concrete-filled double skin steel tubular structure (CFDST) used as a replacement of the conventional steel tube between the water level and the mudline so as to reduce the monopile diameter and thereby reducing the wave loads on the pile. To study the feasibility of this monopile, the NREL 5 MW wind turbine supported by a conventional monopile is selected as a reference and a three-dimensional (3D) finite element model is developed. The natural frequency, the various responses under the serviceability limit state (SLS) and the ultimate limit state (ULS) of the hybrid monopile are presented. Particularly, the effect of varying outer diameter of the CFDST on the structural performance is investigated. By applying a consistent accumulated rotation at the mudline under the SLS, the natural frequency is found to be within a desired range, and an optimized embedded length of the hybrid monopile is determined. The results indicate that the proposed hybrid monopile is able to meet the design requirements for both SLS and ULS and the optimization of pile embedded length leads to an efficient and economic monopile foundation for offshore wind turbines.

1. Introduction

Offshore wind energy has become one of the fastest growing sustainable energy sources. At the end of 2017, the global capacity of offshore wind energy reached over 18.8 GW (GW), nearly 84% of which is located in European countries and the remaining 16% is located mainly in China (GWEC, 2017). The United Kingdom maintains the largest offshore wind market, accounting for over 36% of installed capacity, followed by Germany (28.5%), while China ranks third in the global offshore rankings, accounting for 15% (GWEC, 2017; REN21, 2017). WindEurope expects that by the year 2020, the total European offshore wind capacity will reach 25 GW (GWEC, 2017), while China's offshore wind target will reach 5 GW (Ou et al., 2018). Although offshore wind energy has undergone a rapid development in recent years, the Levelized Cost of Energy (LCOE) for offshore wind turbines is still much higher than that of onshore wind turbines, and it is also significantly higher than the LCOE of conventional power plants, such as energy from coal or gas (Andres et al., 2017; Gentils et al., 2017). If offshore wind turbines are installed in deeper waters and on larger scales, the LCOE will increase further (Schwanitz and Wierling, 2016). This makes it difficult for offshore wind energy to have a competitive price in the energy market (Bocher et al., 2018). For offshore wind turbines, the foundation cost amounts to over 20% of the total capital cost (Gentils et al., 2017; Kim and Kim, 2018). Therefore, there is an urgent need to develop a cost effective foundation for offshore wind turbines.

At present, different types of foundations exist for offshore wind turbines, such as monopiles, tripods, suction caissons, jackets and gravity foundations (O'Kelly and Arshad, 2016). Among them, monopile is the dominant foundation type due to several advantages (O'Kelly and Arshad, 2016; Álamo et al., 2018). Generally, a monopile comprises of a transition piece and a single large diameter open-ended tubular steel pipe that is driven, drilled or vibrated into the seabed. Typically, monopile diameters vary from 4 to 6 m, with the slenderness ratio (ratio between the embedded length and the diameter) between 4 and 8. Most of monopiles are installed in water depths not exceeding 25 m (Murphy et al., 2018; Scharff and Siems, 2013; Negro et al., 2017). As wind farms move further offshore, wind turbines will need to move into much deeper waters and withstand greater loads from waves and winds. As a result, the cost can increase dramatically. Therefore, many studies have been performed with the aim of reducing the cost of monopiles through structural optimization (Gentils et al., 2017; Muskulus and Schafhirt, 2014; Schmoor and Achmus, 2015; Gjersøe et al., 2015; Kallehave et al., 2015; Rad et al., 2014). While the structural optimization may

* Corresponding author.
E-mail address: hwma@sjtu.edu.cn (H. Ma).

https://doi.org/10.1016/j.oceaneng.2020.106963
Received 23 May 2019; Received in revised form 14 November 2019; Accepted 15 January 2020
Available online 23 January 2020

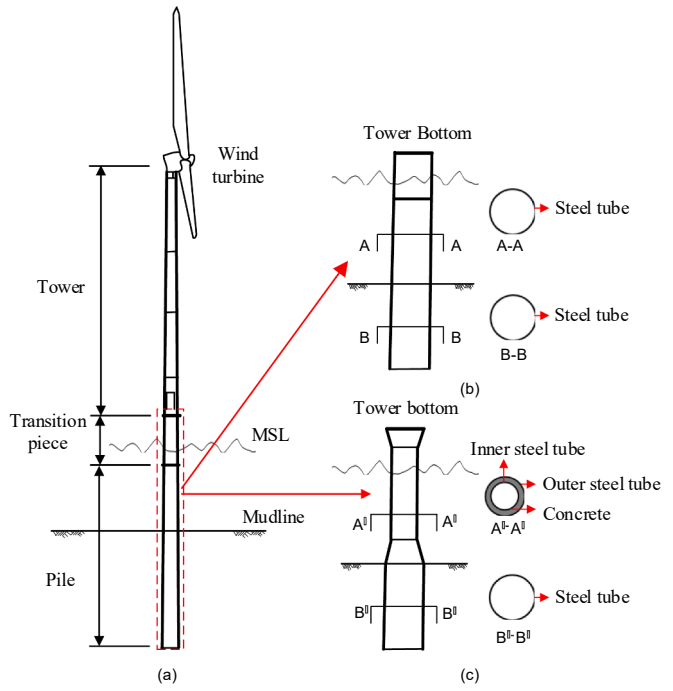

Fig. 1. Schematic illustration of the hybrid and conventional monopile:(a) a monopile supported wind turbine system; (b) conventional monopile; (c) hybrid monopile.

contribute to finding better and more economic solutions, the tendency of rapid increase in monopile cost with the increase in water depth cannot change.

In the design of monopiles, the wave and wind loads are the critical concerns (Arany et al., 2017; Morató et al., 2017; Stansby et al., 2013). Generally, the proportions of wave and wind loads are related to the water depth, and the wave loads become significant for greater water depths and wave heights, which results in a larger area applying wave loads and a larger moment arm for those wave loads, leading to larger mudline stresses in the support structure. Moreover, wave load depends not only on the marine environment, but also on the size of the monopile. According to DNV·GL (2016), the total horizontal force on a monopile due to waves consists of drag force and inertia force. The drag force is directly proportional to the diameter of the monopile whereas the inertia force is directly proportional to the square of the diameter of the monopile. In this respect, a reduction in the diameter of the monopile can reduce the wave load on the monopile.

The main design considerations for a monopile-supported wind turbine include natural frequency, stability, structural strength and fatigue, as well as allowable deformations of the system during operation (DNV.GL, 2016; Velarde, 2016), typically governed by permanent deformations under the SLS and natural frequency (Velarde, 2016; Schmoor and Achmus, 2015; Senanayake, 2016). In order to reduce the wave loads by reducing the diameter of the monopile while still satisfying the design requirements, two measures have been developed: one is to reduce the diameter of the monopile only for the portion between the mudline and the water level, and the other is to use concrete-filled double skin steel tubular structure (CFDST) for that portion of the monopile. CFDST can be regarded as a composite member that is constructed by filling concrete between two concentrically placed steel tubes. It utilizes advantages of both steel and concrete (Han, 2016; Wang et al., 2018; Zhang, 2017), and has been considered as loading bearing elements in some structural engineering applications, such as high piers for bridges, columns for high-rise buildings, support columns for offshore platforms, and transmissions towers (Han et al., 2011; Hassanein et al., 2018; Uenaka, 2016). Compared to pure steel tubular, CFDST

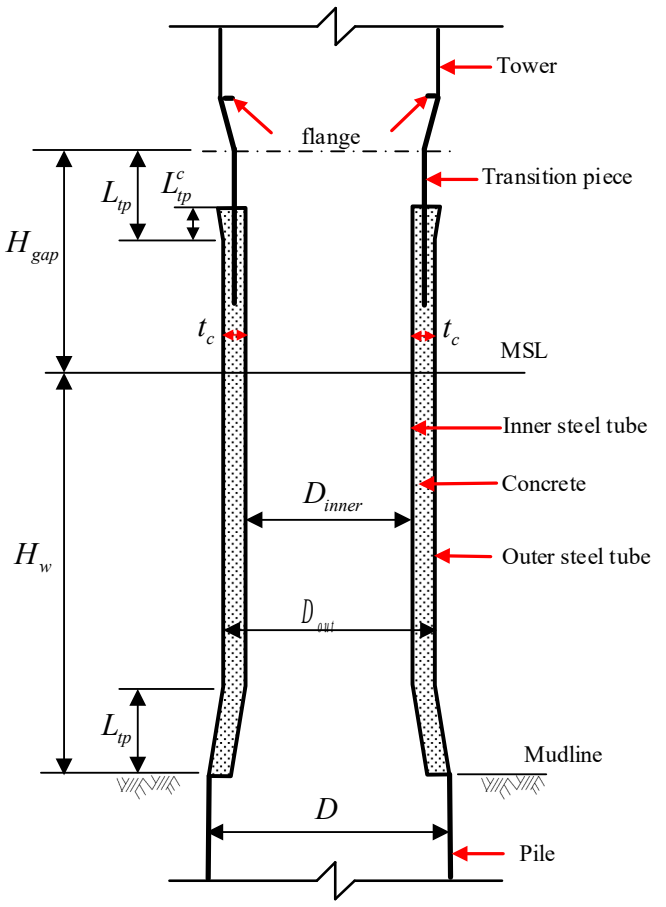

Fig. 2. Details of the CFDST

has a high load-bearing capacity, high rigidity, good energy absorption, high fire resistance, and construction cost-effectiveness (Wang et al., 2018; Li et al., 2018). Therefore, the use of CFDST instead of steel tubular can fulfill the capacity and stiffness requirements with a reduced pile diameter. If ultra-high performance concrete (UHPC) is used instead of normal strength concrete in CFDST, the sectional size of the monopile can be further reduced (Zhang, 2017; Chen et al., 2018).

In this paper, we present a feasibility study using CFDST as part of a monopile foundation for offshore wind turbines. The National Renewable Energy Laboratory (NREL) 5 MW offshore wind turbine (Jonkman et al., 2009) is adopted as a reference model. We investigated the structural responses using the finite element method (FEM) for two foundation types: one is the conventional monopile and the other is the proposed hybrid monopile. Detailed comparisons are made for both the SLS and the ULS. Furthermore, attempt is made to optimize the embedded length of the hybrid monopile using the accumulated rotation at mudline and the natural frequency as design-driving parameters.

2. Concept description for hybrid monopile

The key idea here is to reduce the diameter of the portion of the monopile between the mudline and the water level by replacing the pure steel tubular structure with the CFDST such that the wave load can be reduced. Fig. 1 compares the geometric shapes of conventional and hybrid monopiles. The conventional monopile foundation consists of the pile and the transition piece that connects the pile to the tower. The proposed hybrid foundation consists of the pile and the CFDST. The outer steel tube of CFDST can be fabricated together with the pile through a conical steel tube. In practice, the mechanical shear connectors (e. g. Eom et al., 2019; Shimizu et al., 2013; Thang et al., 2016; Yan

et al., 2016) can be used to achieve the composite action in concrete-filled double skin steel tubes, providing shear resistance and minimizing slip at the steel-concrete interface. A transition piece is set in the hybrid monopile, and grouted to the CFDST. The tower is connected to the transition piece by means of bolts on the top flange. The details of the CFDST are shown in Fig. 2. In this paper, we focused on a feasibility study using CFDSF as part of a monopile foundation for offshore wind turbines. The mechanical shear connector and transition piece are not modeled in detail, and the tower is connected directly to the outer tube of the CFDST. The length of the conical steel tube L_{tp} is set to 7 m (Gentils et al., 2017). The outer diameter of the outer steel tube (D_{outer}) is smaller than the diameter of the pile, and is related to the wall thickness (t_{outer}) as (DNV.GL, 2016):

$$t_{outer} = 6.35 + \frac{D_{outer}}{100} \quad (mm) \tag{1}$$

where D_{outer} is the outer diameter of the outer steel tube of the CFDST. The inner steel tube is like a concrete formwork with a constant wall thickness (t_{inner}=0.02 m), and the outer diameter of the inner steel tube is calculated as follows:

$$D_{inner} = D_{outer} - 2t_{outer} - 2t_c \tag{2}$$

where D_{inner} is the outer diameter of inner steel tube of the CFDST; t_c is the concrete thickness of CFDST.

The total second moment of inertia for a CFDST structure can approximately be estimated by the sum of the second moment of inertia for the outer steel tube, the concrete and the inner steel tube (Huang, 2005). Though CFDST structures have been shown to perform well under a variety of loading conditions (Liang et al., 2019; Li et al., 2019; Wang et al., 2016), there is still limited knowledge regarding the interaction between the concrete and the outer and inner steel tubes, especially for large diameter monopile structures. We used a simple method to approximately estimate the concrete thickness of the CFDST structures. The concrete thickness of the CFDST structure is approximately calculated by an equivalent stiffness between the cross section of the CFDST and the pile of the reference monopile, which is an input for our FEM model. The performance of the CFDST structure under different loading conditions is then examined by the comprehensive FEM analysis not by the simplified method.

$$I_c = \frac{E_s I_{pile} - E_s I_{outer} - E_s I_{inner}}{E_c} \tag{3}$$

$$t_c = \frac{D_{outer} - 2t_{outer} - \left((D_{outer} - 2t_{outer})^4 - \frac{64 I_c}{\pi}\right)^{\frac{1}{4}}}{2} \tag{4}$$

where E_s is the Young's modulus of steel; I_{pile} is the moment of inertia of the pile; I_{outer} is the moment of inertia of the outer steel tube of the CFDST; I_{inner} is the moment of inertia of the outer steel tube of the CFDST; E_c is the Young's modulus of concrete; I_c is the moment of inertia of CFDST concrete.

Like the conventional monopile (Hermans and Peeringa, 2016), the hybrid monopile foundation can be fabricated onshore and transported to designated location using floating method, after which it will be upended and vibro-driving into the seabed to the required depth (Maryruth, 2014). From the viewpoint of fabrication cost, filling the void between the tubes with concrete will lead to thinner shells and smaller diameters of tubes and therefore less steel fabrication costs. Although use of concrete will add extra fabrication cost compared with the traditional pure steel monopile, the tubes themselves act as the concrete formwork and thereby the cost for concrete fabrication is minimal.

Table 1
Main parameters of the NREL 5 MW wind turbine.

Item	Value
Rated Power (MW)	5
Number of blades	3
Rotor diameter (m)	126
Rated wind speed (m/s)	11.4
Cut-in, Rated rotor speed (rpm)	6.9, 12.1
Rotor-nacelle assembly mass (kg)	350,000
Tower base diameter (m)	6
Tower base thickness (m)	0.027
Tower top diameter (m)	3.87
Tower top thickness (m)	0.019
Coordinate location of RNA (x,y,z) (m)	(0.41, 0.00, 1.97)
Moment of inertia of RNA (x, y, z) (kg.m^2)	(4.37, 2.35, 2.54) $\times$ 10^7
Blade mass (kg)	17,740

3. Reference model: NREL 5 MW turbine supported on OC3 monopile

We use the NREL 5 MW wind turbine (Jonkman et al., 2009) as a reference model. This wind turbine has been used as a reference by research teams around the world to quantify the benefits of advanced offshore wind energy technologies (Gentils et al., 2017; Morató et al., 2017). Its main characteristics are described in Table 1. The NREL 5 MW is considered to be supported by a monopile foundation with a water depth of 20 m, designed during the Offshore Code Comparison Collaboration (OC3) project for the International Energy Agency (IEA). The height of the tower is 77.6 m, with a base diameter of 6 m and a top diameter of 3.87 m. The monopile has a length of 56 m and a constant section, with an outer diameter of 6 m and a thickness of 60 mm. The 36-meter monopile was driven into layered sandy soils, and the remaining 20 m was from the seabed up to the sea level. The dimensions of the pile, transition piece and tower and the soil profile are depicted in Fig. 3. The pile is connected to the tower through a transition piece attached by grout at 10 m above the mean sea level (MSL). The tower is bolted together with a transition pie through the internal flange-bolt. The material properties of the pile, tower and transition piece are based on S355 steel, whose density is increased by 8% to account for secondary steel appurtenances, coatings and welds. In this study, a commercial grout material Ducorit D4 is selected; it is commonly used in grouted connections on offshore wind turbines. The mechanical properties of structural steel and grout are summarized in Table 2.

In order to compare the hybrid and conventional monopile foundations, similar wind turbines, towers, site and met-ocean conditions used in the OC3 project are selected for the hybrid monopile study. The distance between the mudline and the tower bottom L_{mp}^{top} is 30 m, and the water depth H_w is 20 m. The diameter ratio λ is defined as the ratio between the outer tube of the CFDST and the outer diameter of the conventional monopile, which is shown as follows:

$$\lambda = \frac{D_{outer}}{D} \tag{5}$$

where D is the outer diameter of the conventional monopile;

It is assumed that a kind of ultra-high performance concrete (UHPC) is used to fill into the gap between the outer and inner tubes of the hybrid monopile. According to some specifications (UHPC, 2017; Jammes et al., 2013), the design parameters for UHPC are listed in Table 2. The thickness of the concrete ring, given in Table 3, is calculated by Eq. (4).

4. Load determination

4.1. Site-specific met-ocean conditions

Offshore wind turbine foundations are designed based on the met-

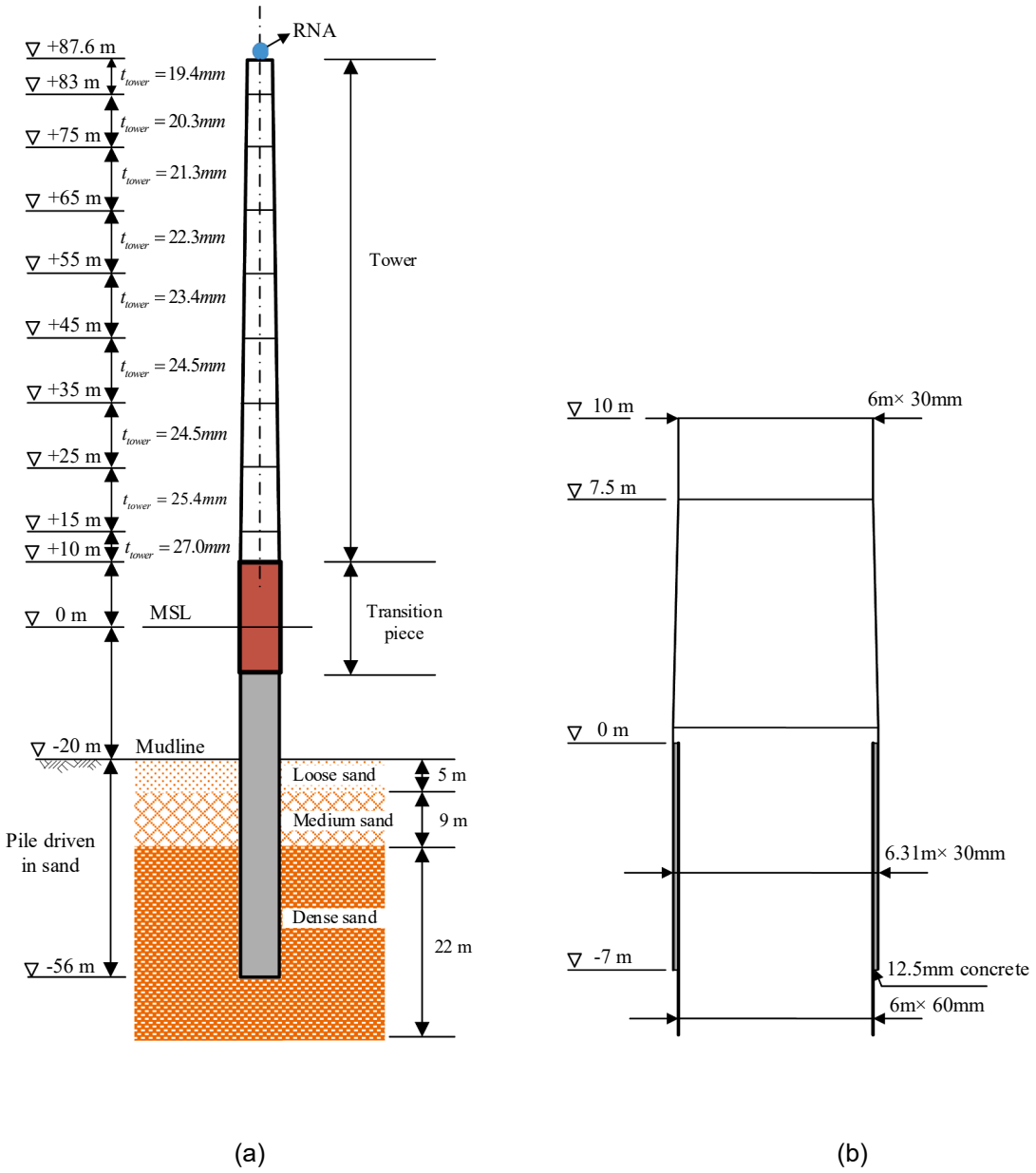

Fig. 3. Geometry: (a) support structure of NREL 5 MW; (b) details of the transition piece.

Table 2
Material properties of steel and grout used in analysis.

Properties	Steel	Grout	UPHC
Young's modulus (GPa)	210	70	50
Poisson's ratio	0.38	0.19	0.2
Density (kg/m^3)	8500	2740	2500
Compressive strength (MPa)	–	200	150
Tensile strength (MPa)	–	10	10
Yield strength (MPa)	355	–	–

Table 3
Parameters of the CFDST monopile used in analysis.

λ	Outer tube (mm)		Concrete ring (mm)	Inner tube (mm)	
	D_{outer}	t_{outer}	t_c	D_{inner}	t_{inner}
0.85	5100	57.35	110	4765.3	20
0.80	4800	54.35	250	4191.3	20
0.75	4500	51.35	510	3377.3	20
0.70	4200	48.35	1000	2103.3	20

ocean conditions which highly depend on the location of the project. The site considered is located at the Dutch sector of the North Sea, 8 km away from the shore of IJmuiden City and is referred to as the NL-1 location in Gentils et al. (2017). The general characteristics of the site met-ocean conditions are summarized in Table 4.

4.2. Permanent loads

Permanent load refers to the weight of the complete structure, which includes the weights of the tower, monopile, Rotor-Nacelle Assembly (RNA) and blades.

Table 4
General information of Site NL-1 (Gentils et al., 2017).

Site NL-1 characteristics	
Water depth (m)	20
Reference wind speed V_{ref} (m/s)	50
50-year extreme 3 s gust wind speed at hub height V_{g50} (m/s)	60
Annual average wind speed V_{ave} (m/s)	10
50-year significate wave height H_{s50} (m)	6.9
50-year pear spectral period T_{s50} (s)	7.7
50-year extreme current speed V_{c50} (m/s)	0.8

4.3. Aerodynamic wind loads

The wind load acting on the turbine rotors is estimated to be (Arany et al., 2017):

$$F_{vh} = 0.5\pi\rho_a R_T^2 V_{hub}^2 C_T \tag{6}$$

where F_{vh} is the wind load acting on the hub in N, R_T is the radius of the rotor in m, V_{hub} is the wind speed at the hub height in m/s, ρ_a is the air density with the value of 1.23 kg/m^3, C_T is the thrust coefficient which is a function of the tip speed ratio and is approximately assumed as 0.5 for $V_{hub} = 11.4\ m/s$ in the present study.

The wind load acting on the turbine tower depends on the wind velocity along the tower. The tower is divided into different segments and the wind load is treated as a concentrated load in each segment. The wind load is calculated as follows (ABS, 2010):

$$F_{tower}^{Z} = 0.5\rho_a C_s A_{tower}^{z} V_z^2 \tag{7}$$

where F_{tower}^{Z} is the wind load acting on the tower of height z in N; A_{tower}^{z} is the wind pressure area on the tower of height z in m^2; C_s is shape coefficient which equals 0.5 for the tubular steel tower; z is the height above the sea water level. The wind profile, V_z, denotes the average wind speed as a function of the height z; in the case of standard wind turbines, the normal wind speed profile is given by the power law (ABS, 2010):

$$V_z = V_{hub}\left(\frac{z}{z_{hub}}\right)^{\alpha} \tag{8}$$

where z_{hub} is the height of the hub; α is the power law exponent which is assumed to be 0.2.

4.4. Wave and current load

Wave loads on slender structural members, such as a cylinder submerged in water, can be predicted by Morison's equation (DNV GL, 2016; Nie and Liu, 2002).

$$F_{wave} = F_M + F_D = \int_{-d_w}^{\eta(t)} C_m\rho\pi\frac{D^2}{4}\ddot{x}dz + \int_{-d_w}^{\eta(t)} C_D\rho\frac{D}{2}\dot{x}|\dot{x}|dz \tag{9}$$

where F_M is the inertia force in N; F_D is the drag force in N; d_w is the water depth in m; C_M is the mass coefficient (2 for a smooth tubular section); C_D is the drag coefficient (1.2) for a smooth tubular section; ρ is the mass density of sea water (1030 kg/m^3); D is the outer diameter of the monopile foundation in m; $\dot{x}$ and $\ddot{x}$ are the wave-induced velocity and the acceleration of water, respectively in the horizontal direction, and $\eta(t)$ is the surface wave profile. The surface wave profile according to linear wave theory is given by (Nie and Liu, 2002):

$$\eta(t) = 0.5h_w\cos(kx - w_w t) \tag{10}$$

$$\dot{x} = \frac{h_w}{T_w}\frac{\pi\cosh(k(Z_2 + d_w))}{\sinh(kd_w)}\cos(kx - w_w t) \tag{11}$$

$$\ddot{x} = \frac{2h_w\pi^2}{T_w^2}\frac{\cosh(k(z_2 + d_w))}{\sinh(kd_w)}\sin(kx - w_w t) \tag{12}$$

where h_w is the wave height in m; k is the wave number in m^{-1}, w_w is the wave frequency in rad/s, T_w is the wave period in s; z_2 is the depth below

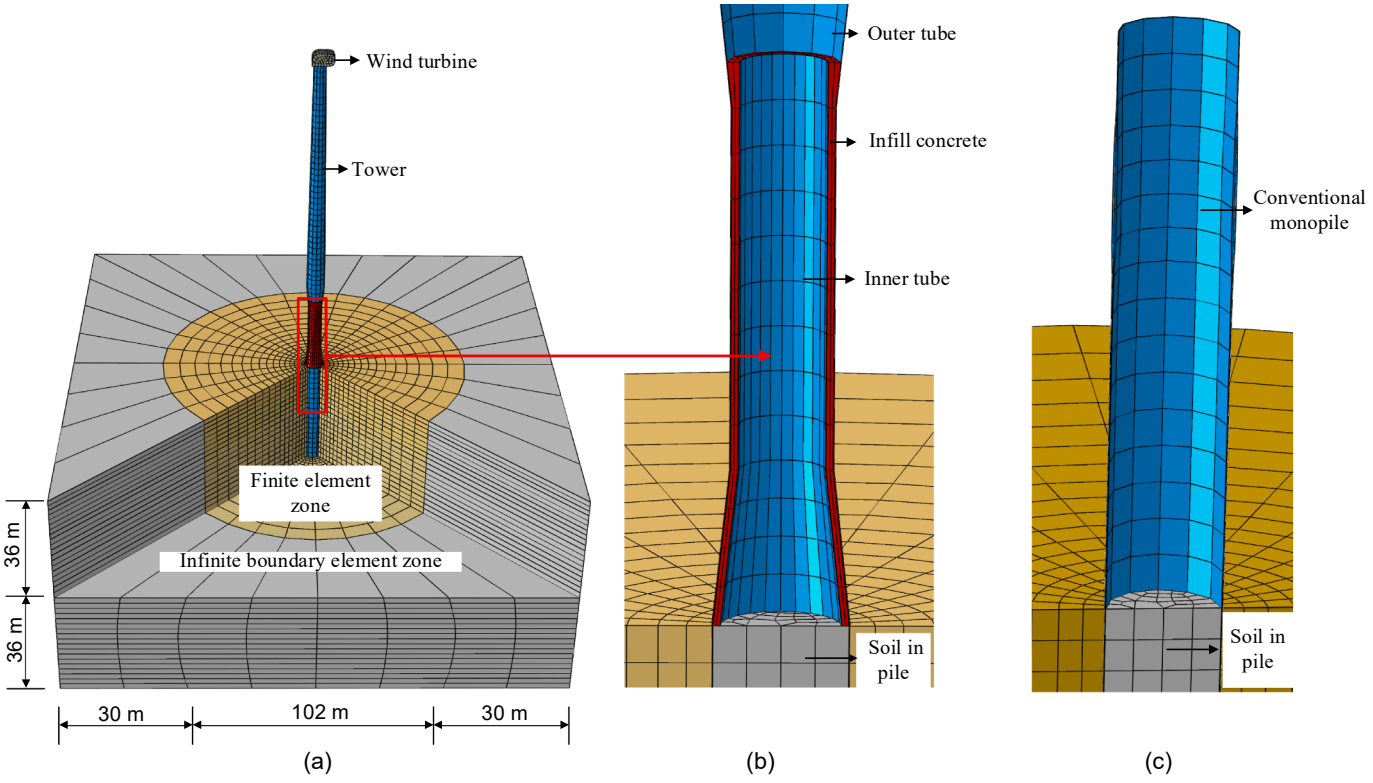

Fig. 4. 3D Finite element model constructed: (a) model as a whole; (b) new monopile; (c) conventional monopile.

Table 5
Properties for different soil layers used in analysis.

Type of sand	Effective unit weight (kN.m^{-3})	Young's Modulus (MPa)	Angle of friction (deg.)	Cohesion (kPa)	Friction coefficient
Loose	10	30	33	2	0.40
Medium	10	50	35	2	0.43
Dense	10	80	38.5	2	0.48

the sea surface in m.

Current structural design models usually involve a simple current profile over depth, using the known current velocity at the water surface as an input parameter. A commonly used method; the power law profile, is adopted here (ABS, 2010). The horizontal current load is estimated as:

$$F_{current} = C_D \rho \frac{D}{2} U_{current}^2 \tag{13}$$

where $F_{current}$ is the horizontal current drag force per unit length in N; $U_{current}$ is the local current velocity in m/s.

This study did not consider other sources of dynamic loads on monopile foundations due to break waves, ice and earthquakes.

4.5. Design load combinations

Two sets of load combinations are used to assess the feasibility of the new monopile foundation. One corresponds to the SLS, one corresponds to the SLS, which includes a rated wind speed of 11.4 m/s under a combined effect of wave and current loads whose return period is 50 years with a load factor of 1.0 for all load categories. The other corresponds to the ULS, and under characteristic load effects similar to the SLS, the load factors are equal to 1.0 and 1.35 for permanent and environmental loads, respectively (DNV.GL, 2016).

5. Numerical modelling and verification

In order to comprehensively analyze the wind turbine-pile-soil system, a three-dimensional (3D) finite element model (FEM) is constructed using the software ABAQUS, as shown in Fig. 4. The key geometric parameters are summarized in Figs. 1 and 2 and Tables 1 and 3 The FEM model consists of seven main components, namely turbine, tower, steel pile, concrete, the soil around the pile, the soil inside the pile (Ma et al., 2017), and infinite boundary elements (Strömblad, 2014). The wind turbine load is applied to the finite element model at tower top. The tower is divided into nine segments and the wind load acts as a concentrated load at each segment. The wave load and current load per unit length are calculated using Eq. (9) and Eq. (13), respectively. They are assumed to act as uniform load on the surface of the monopile foundation in the FE model. Two cases of monopile are investigated for comparison purposes: one is the conventional monopile and the other case is the hybrid monopile.

5.1. Geometric configuration

The size of the soil domain in the FEM is 162 × 162 × 72 m [40, 46]. The lower boundary is fixed against movements in all directions, and the 30 m thick layer of infinite soil creates vertical boundaries that do not reflect shear waves in the soil medium. The continuum element type (C3D8R) is used to model the soil. The outer layer of the soil is modeled using a single layer of solid infinite element (CIN3D8). The tower and the piles are modeled using shell elements (S4R). The concrete is modeled using the continuum element type (C3D8R). The nacelle is modeled as a lumped mass at the top node of the tower with a rotational inertia as specified in Table 1, with contribution from the mass of the rotor, nacelle and blades.

5.2. Material model and properties

The soil is simply represented by a Mohr-Coulomb constitutive model with an elastic-perfectly plastic behavior. The elastic-plastic behavior is mainly defined by cohesion, internal friction angle, dilation angle, modulus of elasticity and Poisson's ratio as shown in Table 5. The piles and tower are assumed to be made of steel material having the typical properties shown in Table 2. Yielding of the steel is not considered in this study. The Concrete Damaged Plasticity model available in ABAQUS is used to model the infilled concrete. This model is a continuum, plasticity-based, damage model for concrete. It is assumed that the two main failure mechanisms are tensile cracking and compressive crushing of the concrete material (ABAQUS, 2013). Four parameters are required to fully describe the yield surface and the flow rule in the three-dimensional stress space, including the dilation angle (ψ), the ratio of compressive strength under biaxial loading to uniaxial compressive strength (f_{b0}/f_b), plastic flow potential eccentricity (ε), and the ratio of the second stress invariant on the tensile meridian to that on the compress meridian (K_c). The values of these parameters are set as 55°, 1.1, 0.1 and 0.67 (Krahl et al., 2018 ; Shafieifar et al., 2017). The concrete between the outer and inner tubes is considered to be confined and an equivalent concrete model is adopted (Ye et al., 2017). The confined concrete is then introduced into ABAQUS. A uniaxial compressive stress (σ) versus strain (ε) relationship is given as follows:

$$y = \begin{cases} 2\chi - \chi^2 & (\chi \le 1) \\ \dfrac{\chi}{\beta_0(\chi-1)^2 + \chi} & (\chi > 1) \end{cases} \tag{14}$$

where $\chi = \varepsilon/\varepsilon_0$; $y = \sigma/f_c^{'}$; $f_c^{'}$ is the cylindrical compressive strength of infill concrete in N/mm^2 and is equal to $0.85f_{cu}$ (f_{cu} is the cube strength of infill concrete); ε_0 and β_0 are determined as

$$\varepsilon_0 = \left(1300 + 12.5 f_c^{'} + 800\xi^{0.2}\right) \times 10^{-6} \tag{15}$$

$$\beta_0 = \left(1.18 \times 10^{-5}\right)^{\left[0.25+(\xi-0.5)^7\right]} \left(f_c^{'}\right)^{0.5} \ge 0.12 \tag{16}$$

where ξ is the confinement factor that can be calculated as:

$$\xi = \frac{A_s f_{ys}}{A_c f_{ck}} \tag{17}$$

where A_s and A_c are the cross-section areas of the outer steel tube and the infill concrete; f_{ys} is the yield stress of the steel; f_{ck} is the characteristic strength of the infill concrete, equivalent to $0.67f_{cu}$.

The infilled concrete between the outer and inner tubes of CFDST under wave and wind loads may be subjected to tension. The simplified stress-strain relationship of infill concrete under tension is assumed as follows. The tensile stress increases linearly with the increase in tensile strain; after concrete cracking it decreases linearly with further increase in strain and approaches zero. The ultimate tensile strain of infill concrete is specified as 10 times the cracking strain, and the cracking strain is set as 0.0001 (Mirzazadeh and Green, 2017).

5.3. Interaction properties

The soil-pile and concrete-pile interactions are modeled using a surface-to-surface contact formulation in ABAQUS/Standard. In this approach, the master surface is defined as a surface belonging to the material that is relatively stiff or has finer mesh geometry, and the slave surface corresponds to the softer material or material with a coarser mesh (Johnson et al., 2001). The pile surface is defined as the master surface, and the soil and concrete surfaces in contact with the pile are defined as the slave surface. In the normal direction, the interface contact is assumed to be a "hard" contact, and no separation was allowed. When the surfaces are in contact, any contact pressure can be

Table 6
Computed and measured natural frequencies.

FEM	Measurements (Shirzadeh et al., 2013)	
0.3657 Hz	Over speed stop 0.3529 Hz	Ambient excitation 0.3565 Hz

transmitted between them. The surfaces are separated if the contact pressure is reduced to zero. In the tangential direction, the classical isotropic Coulomb friction model is used to simulate the shear-resistance interaction (Johnson et al., 2001; Strömblad, 2014; Sheng et al., 2005). The friction coefficient (μ) for the interface between the pile and the soil is simply taken as $\mu = \tan\left(\frac{2}{3}\varphi\right)$, where φ is the friction angle of the soil. For the interface between the pile and the concrete, values of 0.2–0.3 are typically used as they provide acceptable results compared to experiments. In this study, the friction coefficient (μ) between the pile and the concrete is selected as 0.3 (Hassanein et al., 2018).

5.4. Model validation

For the reference wind turbine model compatible with the conventional monopile foundation, our FEM is validated by comparing the computed results with the field measurements at natural frequencies (Shirzadeh et al., 2013) and with full-scale lateral loading test data (Hokmabadi et al., 2012).

Shirzadeh et al. (2013) reported the field measurements of the first fore-aft mode frequency for a 3 MW offshore wind turbine supported by a monopile in the Belgian North Sea. The overspeed stop test and ambient excitation were used to estimate the first for-aft mode frequency. Based on the available soil, monopile, tower and turbine data from Shirzadeh et al. (2013), a 3D FEM is developed using ABAQUS. The

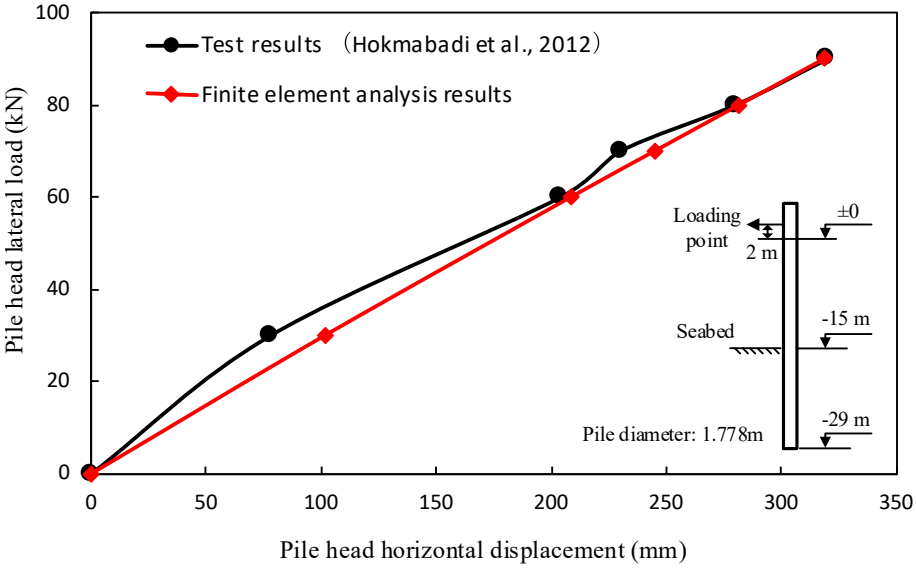

Fig. 5. Comparison of field test results with finite element analysis results.

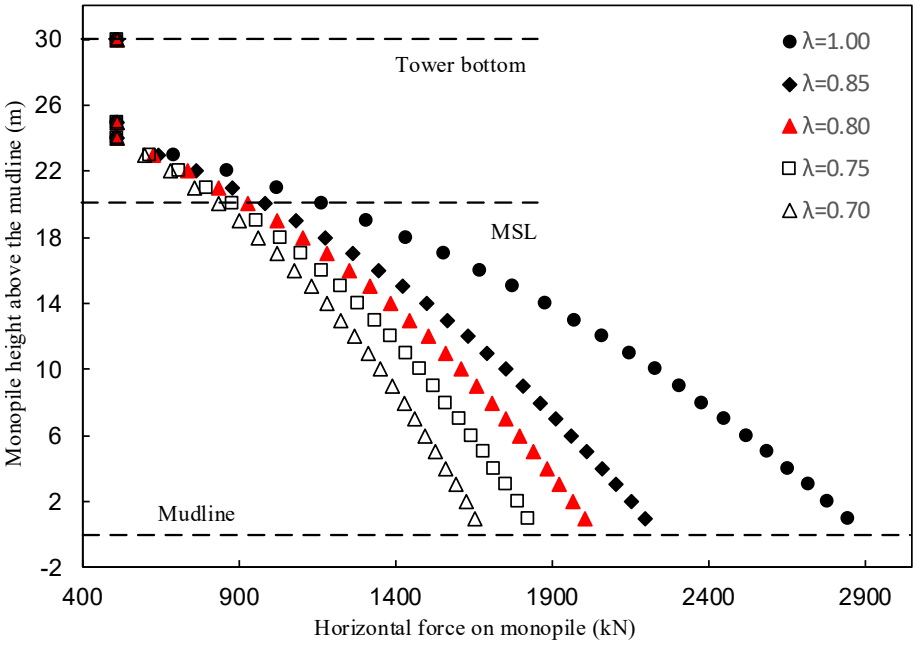

Fig. 6. Computed horizontal forces on monopile under the SLS.

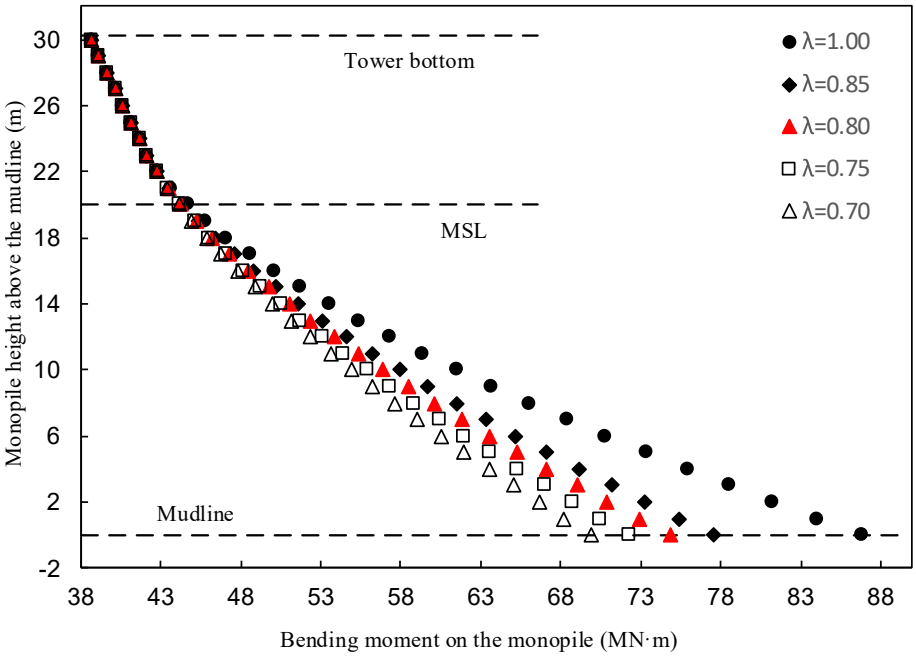

Fig. 7. Computed bending moments on monopile under the SLS.

comparative results of the finite element analysis with the reported results are shown in Table 6. It can be seen that the result of the finite element analysis is in good agreement with that of the reported results.

Hokmabadi et al. (2012) reported full-scale load tests to investigate the behavior of offshore monopiles in marine sandy soils. The length and diameter of the monopile were approximately 34 m and 1.78 m, respectively. A 3D FEM similar to that developed in the present study is established using ABAQUS for this monopile-supported wind turbine, with soil and pile properties taken from Hokmabadi et al. (2012). The result of pile head load versus pile head deflection obtained from the finite element analysis is presented in Fig. 5, showing a reasonably good agreement.

6. Results and discussion

This section presents the numerical results for hybrid and conventional monopile foundations. The results include the horizontal loads, the natural frequency, the lateral displacement and the rotation of the monopile under the SLS, the maximum von Mises stress of the monopile under the ULS, the optimum of the embedded length and materials cost of the hybrid monopile. The outer diameter ratio λ is a key design parameter that plays an important role in the performance of the hybrid monopile. To investigate its influence, λ was chosen to be 1.0, 0.85, 0.8, 0.75 and 0.7.

6.1. Horizontal load and bending moment along monopile

Using the load calculation methods described above, the wind, wave and current loads are determined based on the met-ocean conditions at site NL-1. The total horizontal load and the bending moment along the monopile with different λ values under the SLS are plotted in Fig. 6 and Fig. 7, where the horizontal axis represent the cross-sectional load and bending moment at different levels of the monopile, respectively. It can be seen that the change in λ directly influences the horizontal load and bending moment profiles along the monopile, and they all have a decreasing tendency as λ decreases. At mudline, as the λ decreases from 1.0 to 0.7, the horizontal load and the bending moment are reduced by almost 41.8 and 19.5%, respectively. It is indicated that the reduction of the pile diameter can effectively reduce the total external load for the monopile.

Table 7
Natural frequencies.

Natural frequency	$\lambda = 1.0$	$\lambda = 0.85$	$\lambda = 0.80$	$\lambda = 0.75$	$\lambda = 0.70$
f_1	0.2332	0.2256	0.2231	0.2218	0.2167
f_2	1.4471	1.4485	1.4446	1.4439	1.3949

6.2. Natural frequency

The natural frequency of an offshore wind turbine is a major design driver for the monopile support structure, since it defines the dynamic behavior of the structure (Velarde, 2016). The overall natural frequency must not coincide with the excitation frequencies due to wind and waves. In design practice, the first natural frequency (f_1) lies between the frequencies 1P (rotor speed frequency) and 3P (blade passing frequency), which is called the "soft-stiff" design (O'Kelly and Arshad, 2016). Based on the rotor speeds as shown in Table 1, the first natural frequency (f_1) is required to be in a range between 0.202 Hz (1P) and 0.345 Hz (3P) to avoid resonance. If the calculation uncertainties ±5% are included (DNV.GL, 2016), the above range goes from 0.212 Hz to 0.328 Hz. The linear perturbation method is used to determine f_1 and f_2. As shown in Table 7, all f_1 fall within the allowable "soft-stiff" region (1P–3P), and all f_2 fall well above the maximum limit of the 3P operational (0.636 Hz). Consequently, the hybrid monopile can be considered safe from resonance or resonance-related effects. In Table 7, as λ is reduced from 1.0 to 0.7, f_1 is reduced from 0.233 Hz to 0.217 Hz, and f_2 is reduced from 1.447 Hz to 1.395 Hz, by about 6.9% and 3.6%, respectively. These changes are due to the fact that the stiffness remains constant as λ decreases from 1.0 to 0.7 but the mass of the monopile increases due to the use of CFDST.

6.3. Pile stress distribution under the ULS

The stress distribution of the outer steel tube is shown in Fig. 8. The maximum von Mises stresses of the outer steel tube of the hybrid monopile are 142.7, 127.8, 124.3 and 105.5 MPa for λ = 0.7, 0.75, 0.8

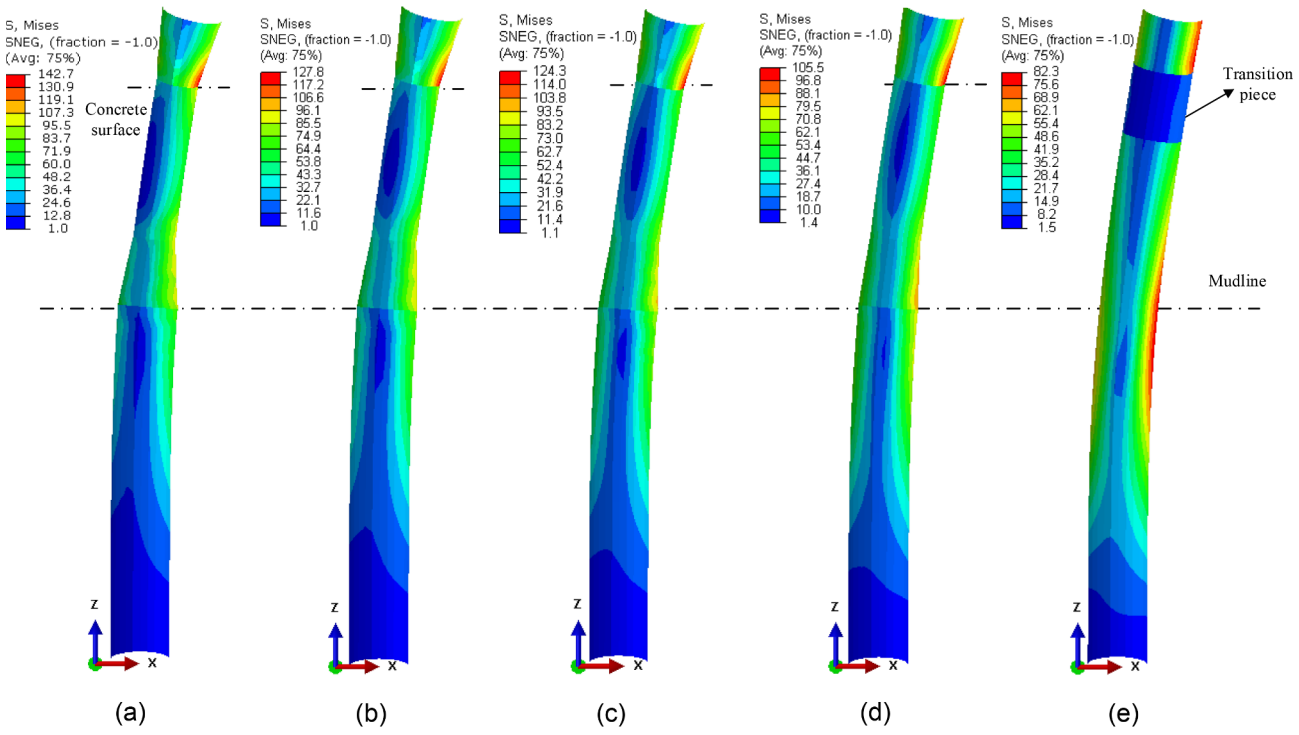

Fig. 8. Von Mises stress distribution of the outer steel tube: (a) $\lambda = 0.7$; (b) $\lambda = 0.75$; (c) $\lambda = 0.8$; (d) $\lambda = 0.85$; (e) $\lambda = 1.0$

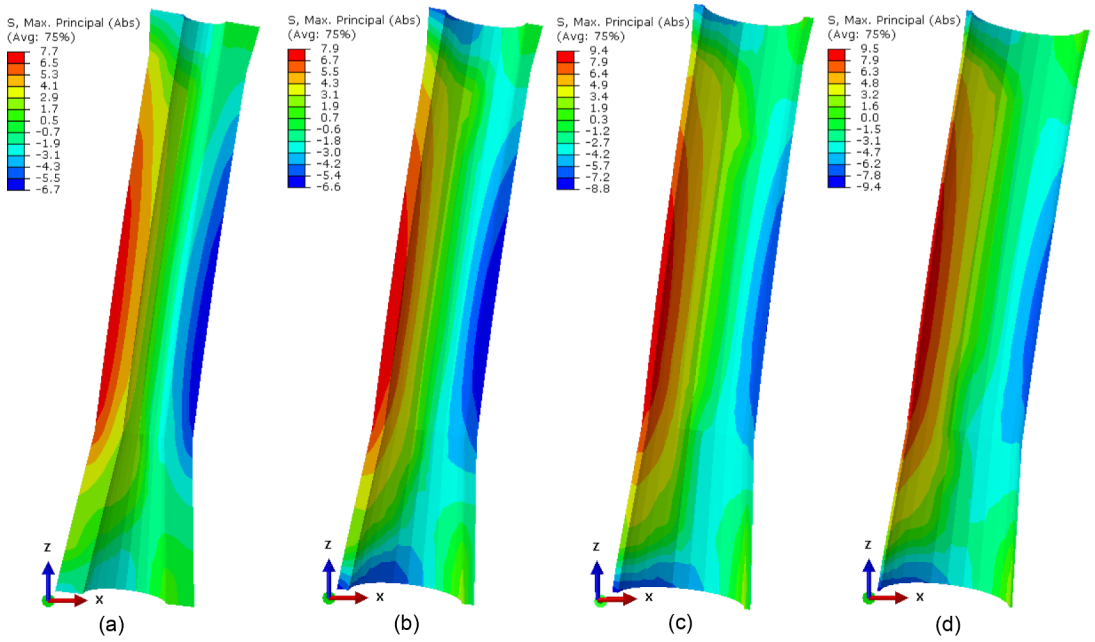

Fig. 9. Tensile and compressive stress distribution of the concrete between outer and inner steel tube: (a) $\lambda = 0.7$; (b) $\lambda = 0.75$; (c) $\lambda = 0.8$; (d) $\lambda = 0.85$

and 0.85, respectively, which are located at the cross-section above the top surface of the concrete. These values are below the permissible value of 355 MPa. The maximum von Mises stress of the pile for $\lambda = 1.0$ is 82.3 MPa, which is located near the mudline. Fig. 9 shows the tensile and compressive stress distribution of the concrete. The maximum compressive stresses are far below the compressive strength of the UHPC (150 MPa). The maximum tensile stresses are 7.7, 7.9, 9.4 and 9.5 MPa for $\lambda = 0.7$, 0.75, 0.8 and 0.85, respectively, which are less than the tensile strength of UHPC (10 MPa), and therefore the concrete will not crack. The stress distributions of the inner steel tube of the hybrid monopile are depicted in Fig. 10. The maximum cross-section von Mises stresses are 15.8, 27.2, 35.6 and 49.4 MPa for $\lambda = 0.7$, 0.75, 0.8 and 0.85, respectively, which are far less than the permissible value of 355 MPa. Therefore, the CFDST structure is safe under the ULS.

6.4. *Global buckling check under the ULS*

For the ultimate strength of the monopile, the buckling stability should be checked using a rational and justifiable engineering approach (DNV.GL, 2016). Buckling refers to sudden collapse of the structure

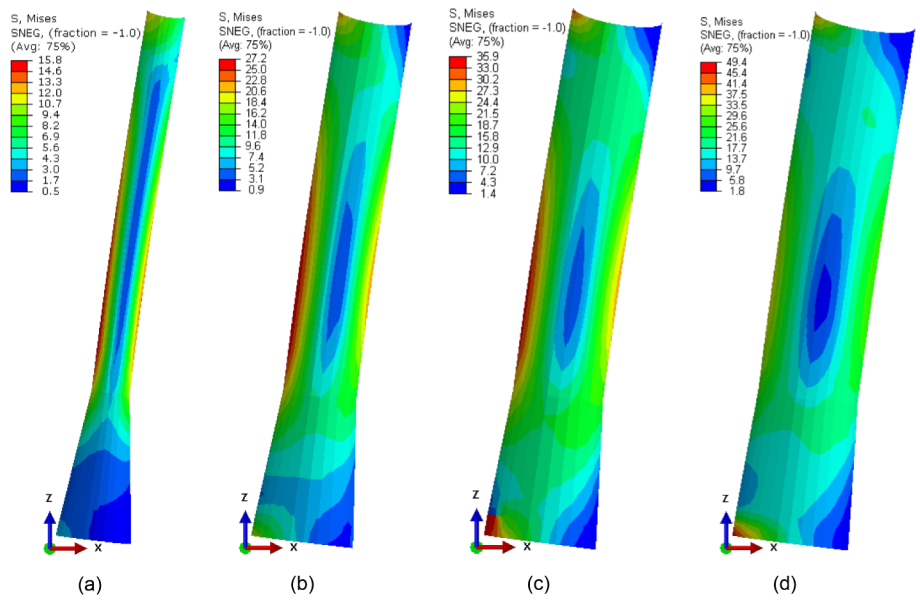

Fig. 10. Von Mises stress distribution of the inner steel tube: (a) λ = 0.7; (b) 0.75; (c) λ = 0.8; (d) λ = 0.85

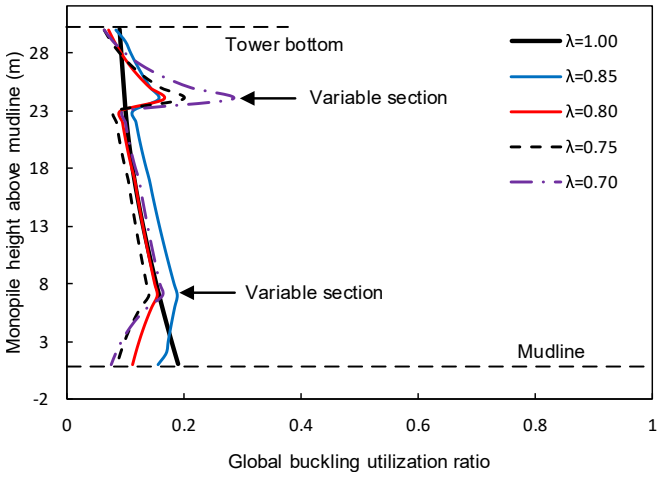

Fig. 11. Global buckling check for monopiles under the ULS.

either globally or locally. For the hybrid monopile, the mechanical shear connectors should be used to achieve the composite action in concrete-filled double skin steel tubes, and can be beneficial for local buckling prevention (Eom et al., 2019); the local buckling of both steel tubes can be effectively constrained due to the presence of infilled UHPC concrete (Wang et al., 2019). Therefore, the local buckling will be complicated and delayed, such detailed analysis does not included in this paper. The global buckling is checked according to Standard for design of steel structures (GB 50017–2017) and Technical specification for concrete-filled double skin steel tubular structures (CCES, 2018). As shown in Fig. 11, the global buckling utilization ratios of the conventional and novel monopiles are far less than 1.0. This indicates the present hybrid monopile is not likely to suffer from global buckling failure.

6.5. Pile deformation under the SLS

Figs. 12 and 13 show the comparison of lateral deflection and rotation along the pile for different λ values under the SLS, respectively. It is obvious that its lateral deformation decreases when λ decreases. As λ decreases from 1.0 to 0.7, the lateral deflection and the rotation in the mudline are reduced from 19.3 to 12.8 mm (about 33.7%) and from 0.104 to 0.072° (about 30.8%), respectively. The critical depth as a transition point (from positive to negative displacement) is also reduced from −19 to −17 m. In addition, the lateral deflection and rotation at the pile toe is also reduced from −1.52 to −1.07 mm (about 19.6%) and from 0.0047 to 0.0021° (about 55%). These are attributed to the reduction of horizontal wave loads by reducing λ.

6.6. Permanent accumulated rotation at mudline under the SLS

In most cases, the permanent deformation tolerance of the pile under the SLS is design-driving for monopiles in sandy soils (Velarde, 2016; Schmoor and Achmus, 2015; Senanayake, 2016). The deformation tolerances are usually given in the design basis and are often specified in terms of maximum tolerance rotations of the pile at the mudline in a vertical plane. Typically, the tolerance for the total rotation is 0.5° and the installation tolerance is 0.25°, then the limit for permanent accumulated rotation becomes 0.25° for SLS loads throughout the design life (DNV.GL, 2016).

According to Schmoor and Achmus (2015), the accumulated rotation of the pile at mudline can be estimated with the empirical exponential approach as follows:

$$\theta_N = \theta_1 \zeta_{SDM} \tag{18}$$

where θ_N is the pile accumulated rotation by N cycles of lateral load; θ_1 is the rotation obtained in the first loading cycle, which can be calculated in a static analysis under the SLS loads; ζ_{SDM} is derived from the Stiffness Degradation Method (SDM) presented in Kuo (2008) and Achmus et al. (2009), which is

$$\zeta_{SDM} = e^{(A-1.208)\ln\left(\frac{H\left(h+L_{pile}\right)}{\gamma' D L_{pile}^3}\right)+B-0.588} \geq 1 \tag{19}$$

where L_{pile} is the pile embedded length in m; H is the horizontal force in kN; h is the moment arm in m (31.6 m, 36.5 m, 38.6 m, 40.9 m and 43.6 m for λ = 1.0, 0.85, 0.8, 0.75 and 0.7, respectively); $\gamma' \approx 10\ kN/m^3$ is the soil effective unit weight; A and B are regression parameters and take values of 1.361 and 1.331 for the SLS (number of cycles N = 100) according to Schmoor and Achmus (2015) and Barari et al. (2017).

The pile permanent accumulated rotation θ_N at mudline under the SLS loads is presented in Table 8. It can be clearly seen that the overall

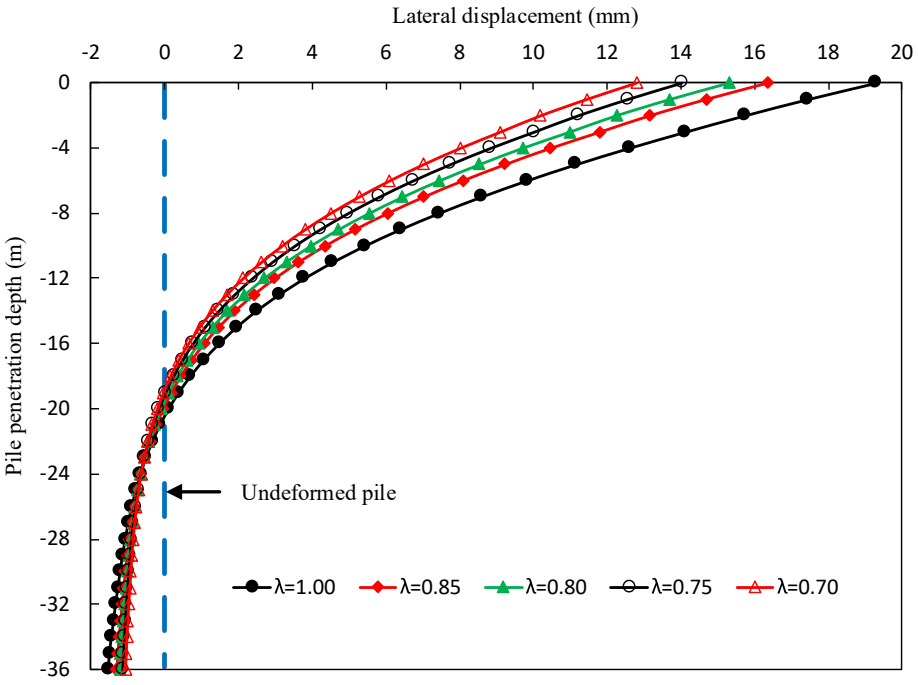

Fig. 12. Distribution of pile deflection under the SLS.

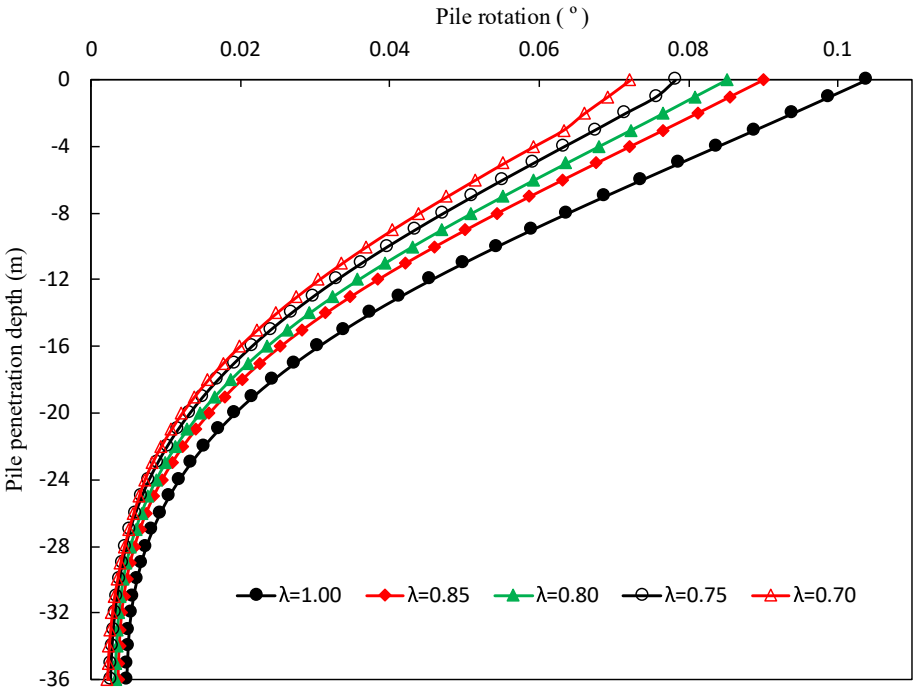

Fig. 13. Distribution of pile rotation under the SLS.

Table 8
Pile rotation at mudline under the SLS.

Pile rotation	$\lambda = 1.0$	$\lambda = 0.85$	$\lambda = 0.80$	$\lambda = 0.75$	$\lambda = 0.70$
θ_1 (°)	0.104	0.090	0.085	0.078	0.072
ζ_{SDM}	1.395	1.356	1.343	1.330	1.317
θ_N (°)	0.145	0.122	0.114	0.104	0.095

trend of θ_N decreases with λ. As λ decreases from 1.0 to 0.7, θ_N reduces from 0.145° to 0.095° (about 34.5%). Therefore, it is possible to optimize the geometry of the monopile while maintaining a similar accumulated rotation at mudline with that of the conventional monopile (λ=1.0). This can lead to a more economical design.

7. Embedded length optimization for hybrid monopile

To compare the embedded length between the hybrid monopile and the conventional monopile (OC3), two major design drivers are selected for monopile foundation: one is the pile permanent accumulated

Table 9
Monotonic rotation (°) at the mudline of the monopile with different.**β**

β	λ = 0.85	λ = 0.80	λ = 0.75	λ = 0.70
0.6	0.1095	0.1074	0.0995	0.0911
0.7	0.0938	0.0924	0.0866	0.0786
0.8	0.0930	0.0883	0.0817	0.0744
0.9	0.0912	0.0861	0.0798	0.0731
1.0	0.0900	0.0851	0.0783	0.0722

rotation (θ_N) at mudline under the SLS; the other is the natural frequency (f_1.f_2) of the overall support structure. During the comparison process, θ_N remains similar between the hybrid and the conventional monopile; f_1 lies in the desired range, I.e. between 0.212 Hz and 0.328 Hz; f_2 falls above the maximum limit of the 3P operational; the diameter and wall thickness of the embedded pile of the hybrid monopile remain constant. Several embedded pile length ratio β = 0.9, 0.8, 0.7 and 0.6 are selected.

$$\beta = L_{pile} \Big/ L_{pile}^{OC3} \tag{20}$$

where L_{pile}^{OC3} = 36 m is the pile embedded length for the reference model.

For different cases of β, a total of 20 (4 × 5) finite element models are established for calculating the pile rotation in the first loading cycle (θ_1), as shown in Table 9. When β is reduced from 1.0 to 0.6, the value of θ_1 is increased by nearly 22, 26, 27 and 26.2% for λ values of 0.85, 0.8, 0.75 and 0.7, respectively. The pile accumulated rotations with different β are calculated with Eqs. (18) and (19). As shown in Fig. 14, θ_N at mudline increases with decreasing β. Specifically, when λ = 0.85, 0.80, 0.75 and 0.70, β decreases from 1.0 to 0.6, and θ_N increases by 48, 54, 55.7 and

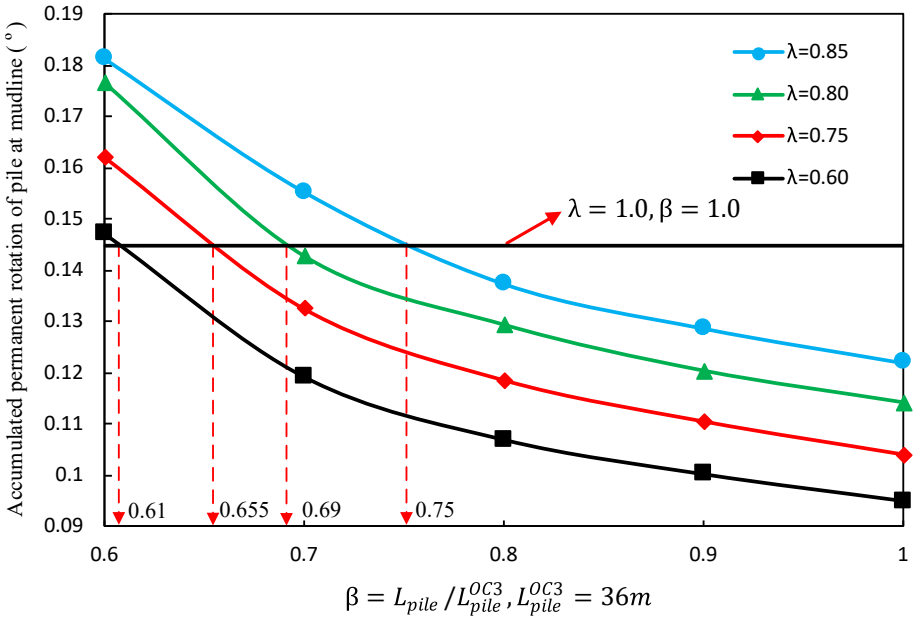

Fig. 14. Pile accumulated rotation at mudline under the SLS.

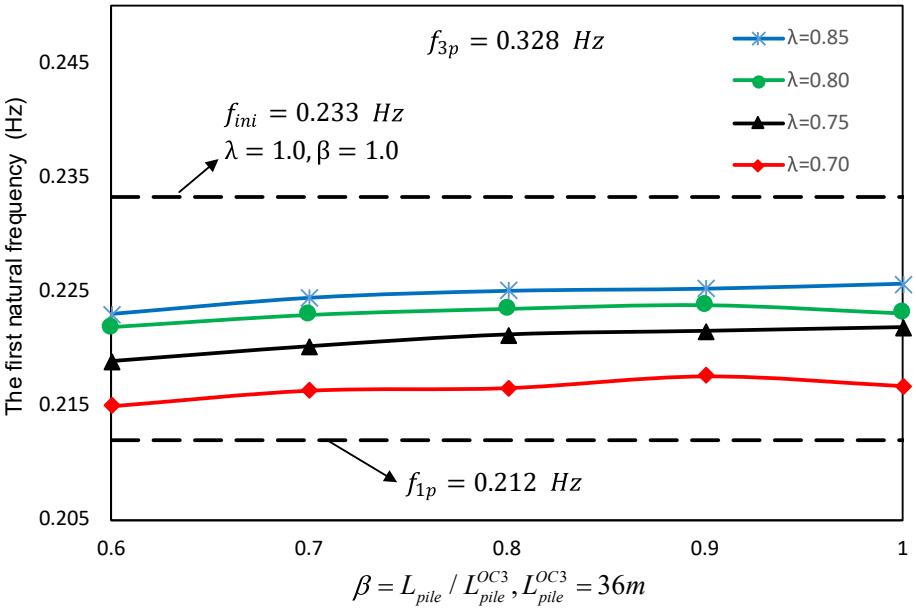

Fig. 15. Values of the first natural frequency under different **β** and **λ** values.

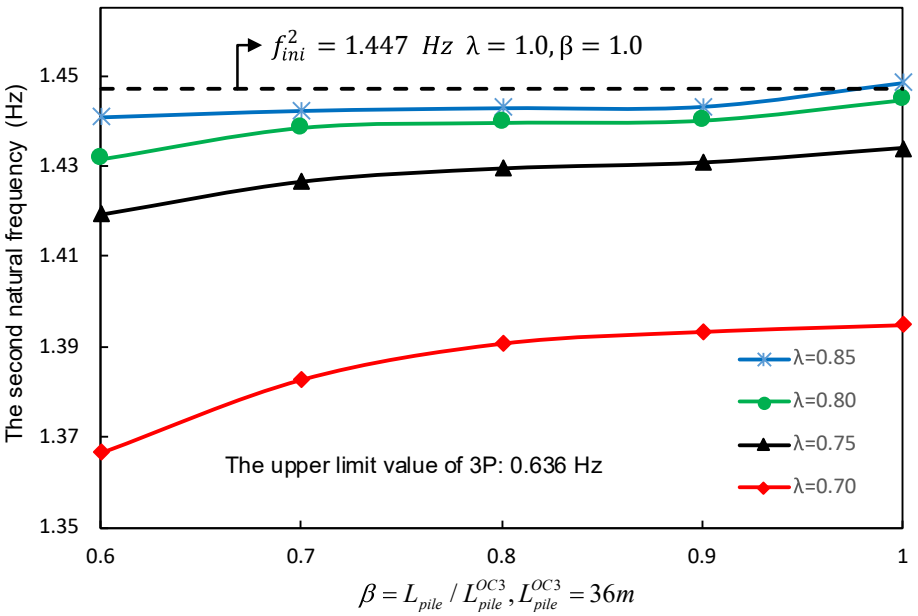

Fig. 16. Values of the second natural frequency under different **β** and **λ** values.

55%, respectively. This means that the embedded pile length has a significant impact on the pile accumulated rotation. The conventional monopile is taken with $\lambda = 1.0$ and $\beta = 1.0$, and in this case the accumulated permanent rotation at mudline is 0.145°. For the same accumulated permanent rotation at mudline, values of λ and β are varied for hybrid monopile and an optimum condition is achieved, as shown in Fig. 14. The results show that the equal accumulated permanent rotation is achieved for $\lambda = 0.85$ at 75% of the embedded pile length. Similarly, for $\lambda = 0.80$, 0.75, and 0.6, the same accumulated permanent rotation is achieved at 69, 65.5, and 61% of the embedded pile length, respectively.

Fig. 15 shows the first natural frequency of the NREL 5 MW offshore wind turbine supported by the hybrid monopile foundation. The reduction in β from 1.0 to 0.6 has little effect on the first natural frequency under different λ conditions. The first natural frequency is less than that of the comparative model (OC3, $\lambda = 1.0$, $\beta = 1.0$), on decreasing by 3.7, 4.4, 5.6 and 7.7% for $\lambda = 0.85$, 0.80, 0.75 and 0.70, respectively, which are within the desired range of 0.212 Hz and 0.328 Hz. As shown in Fig. 16, the second natural frequencies are all above the above the maximum limit of the 3P operational (0.636 Hz), and are less than that of the comparative model.

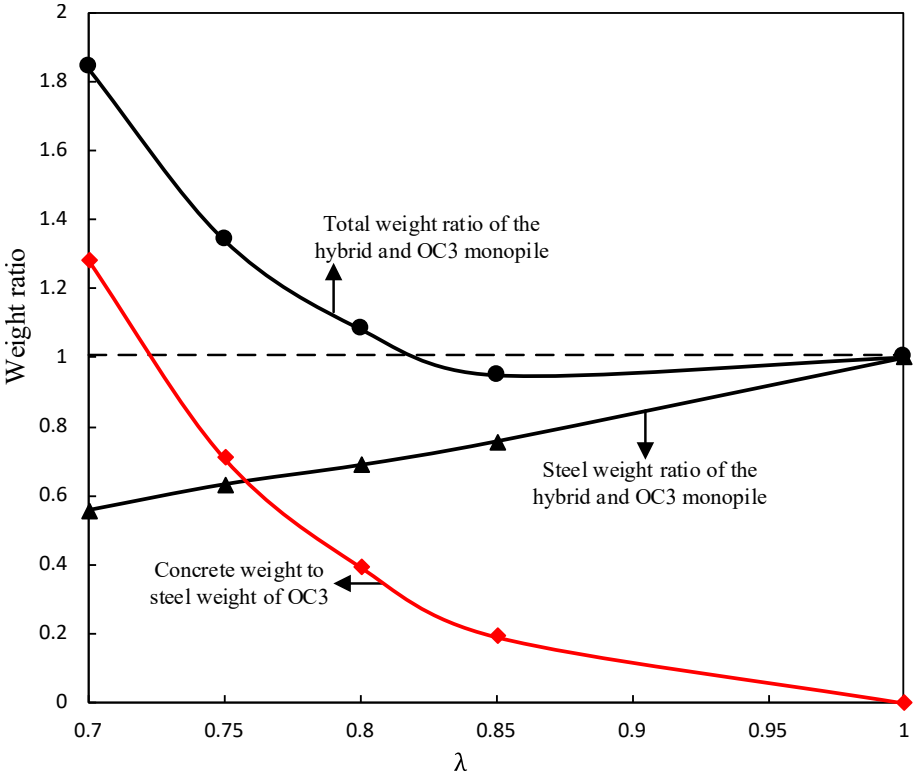

Fig. 17. Weight ratio of the hybrid and OC3 monopile.

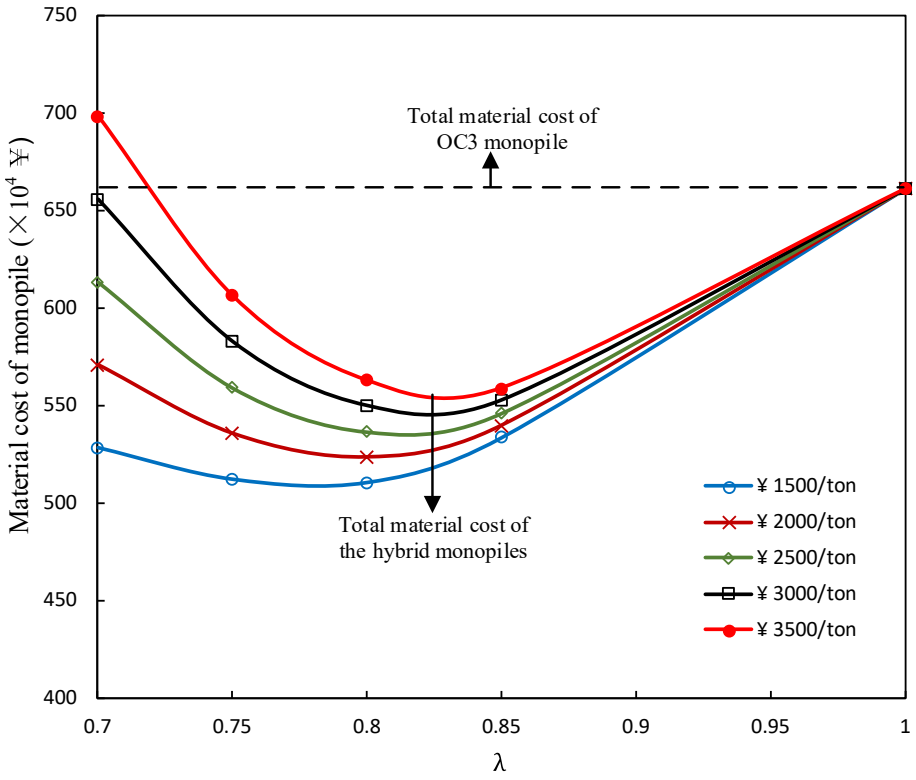

Fig. 18. Total material cost of the hybrid and OC3 monopile.

8. Cost comparison for hybrid monopile and OC3 monopile

In general, costs for monopile foundation include those for materials, fabrication, installation, transport and maintenance. Among them, the material weights and costs are relatively straightforward to estimate, but costs related to installation, manufacturing and transport (Muskulus and Schafhirt, 2014) are complicated and depend on many factors. In the present study we focus mainly on the comparison of costs of materials for the hybrid type and the conventional type of monopile. In doing this, a steel weight ratio w_s is defined as the ratio between the weight of the hybrid monopile (w_{steel}^{novel}) and the weight of the conventional monopile (w_{steel}^{OC3}):

$$w_s = \frac{W_{steel}^{novel}}{W_{steel}^{OC3}} \tag{21}$$

For steel, a price of 10000 ¥/ton including the cost for raw material and labor (MIIC, 2018) is supposed. Ultra-high performance concrete is much more expensive than normal concrete and the price depends on the formulation of products for various applications (Christopher et al., 2017); the price also varies in different markets and regions around the world (NPCA, 2015). According to Xu (2015), the unit price of UHPC is from ¥1000/ton to ¥1200/ton; the unit price of Nanodur® Compound 5941 available in the market is about ¥2800/ton to ¥3420/ton (~€366/ton to €446/ton) (UHPC, 2017). Therefore, a range of values of unit price for UHPC (¥1500/ton to ¥3500/ton) is used in the cost estimation. The total material cost C_{tot} is calculated as:

$$C_{tot} = C_c w_c + C_s w_s \tag{22}$$

where C_c and w_c are the unit price and weight of UHPC, respectively; C_s and w_s are the unit price and weight of steel, respectively.

Fig. 17 illustrates the effects of λ on the material weight of the hybrid monopile. Compared to the conventional monopile, the total weight of the hybrid monopile increases nearly by 1.85 times while the steel weight ratio w_s decreases by 55.7% as λ decreases from 1.0 to 0.7. As a result, the total material cost (C_{tot}) of the hybrid monopiles is less than that of the convention monopile in most situations. Fig. 18 shows that C_{tot} increases with the increase of the unit price of UHPC (C_c) and the magnitude of increase becomes larger as λ decreases. For example in the case of C_c = ¥3500/ton, the total material cost for the hybrid monopile is reduced approximately 13.6%, 18.9%, 20.7% and 18.3% for λ = 0.7, 0.75, 0.8 and 0.85, respectively. This suggests that the hybrid type of monopile is a cost-effective alternative to the conventional type of monopile for offshore wind turbines.

9. Conclusions

This paper presents a hybrid type of monopile foundation for offshore wind turbines and investigates its feasibility by a comprehensive numerical analysis. The NREL 5 MW wind turbine supported by a conventional monopile is used as a reference model for comparison. The natural frequency and the structural responses under the SLS and ULS conditions are computed and compared. The main results are summarized as follows:

(a) Compared to the conventional monopile (OC3λ = 1.0), the horizontal load at mudline for the hybrid monopile can be reduced by 22.8, 29.5, 35.9 and 41.8%, respectively, at λ values of 0.85, 0.8, 0.75 and 0.7, and the bending moment can be reduced by 10.7, 13.7, 16.7 and 19.5%, respectively. This indicates that the hybrid monopile can effectively reduce the total external load on the pile.

(b) The first natural frequency of the system decreases by approximately 7% as λ decreases from 1.0 to 0.7 and the natural frequencies at various λ values remain between the frequencies 1P (rotor speed frequency) and 3P (blade passing frequency). This is due to the fact that the cross-sectional stiffness remains unchanged for the hybrid type and the conventional type of monopile but the mass of the hybrid monopile increases.

(c) Under the ultimate limit state, the maximum stresses in the steel tube pile and in the filled concrete do not exceed the permissible stresses.
(d) Under the serviceability limit state, the permanent accumulated rotation at mudline is reduced from 0.145 to 0.095° (about 34.5%) as λ decreases from 1.0 to 0.7. This is mainly due to the reduction of wave loads on the hybrid monopile. Considering that the permanent accumulated rotation under the SLS is a major design driver for monopile foundation, the embedded pile length can possibly be optimized to achieve a more economical design.
(e) Using the proposed optimization criteria, the embedded length of the hybrid monopile can be reduced by 25, 31, 34.5 and 39% for λ being 0.85, 0.8, 0.75 and 0.7, respectively. This indicates that the steel weight and the relevant cost can be significantly reduced. The hybrid monopile therefore is a cost-effective alternative to the conventional monopile for offshore wind turbines.

Last but not least, it should be noted that a number of issues need to be studied for practical use of the new type of monopile, such as the detailed connection between the concrete and the steel tube, the fatigue performance of the concrete and the nonlinear wave theory used for prediction of wave loads on the hybrid monopile for extreme wave conditions.

Author contributions

Hongwang Ma: Concept of the new hybrid monopile, Methodology, Finite element model and analysis, Data curation, Writing- Original draft preparation. Jun Yang: Methodology, Writing- Reviewing and Editing.

Declaration of competing interest

The authors declare that they have no known competing financial interests or personal relationships that could have appeared to influence the work reported in this paper.

Acknowledgments

The authors wish to acknowledge the financial support provided by the National Basic Research Program of China (973 Program, No. 2014CB046200) and the Visiting Professorship awarded by Shanghai Jiao Tong University, China.

Notation

The following symbols are used in this paper

A_c	cross-section area of the infill concrete
A_s	cross-section area of the outer steel tube
A_{tower}^{z}	wind pressure area on the tower of height z
C_D	drag coefficient
C_M	mass coefficient
C_s	shape coefficient
C_T	thrust coefficient
CFDST	concrete-filled double skin steel tubular structure
d_w	water depth
D	outer diameter of the conventional monopile
D_{inner}	inner diameter of the inner steel tube of the innovative monopile
D_{outer}	outer diameter of the outer steel tube of the innovative monopile
E_c	Young's modulus of concrete
E_s	Young's modulus of steel
f_1	First natural frequency
f_2	Second natural frequency
$f_c^{'}$	compressive strength of infill concrete
f_{ck}	characteristic strength of the infill concrete
f_{cu}	cube strength of the infill concrete
f_{ys}	the yield stress of steel
$F_{current}$	horizontal current drag force per unit length
F_D	drag force
F_M	inertia force
F_{tower}^{Z}	wind load acting on the tower of height z
F_{vh}	wind load acting on the hub
g	acceleration of gravitation
h_w	wave height
I_c	concrete section moment of inertia
I_{inner}	inner steel tube section moment of inertia of the innovative monopile
I_{outer}	outer steel tube section moment of inertia of the innovative monopile
I_{pile}	pile section moment of inertia of conventional monopile
k	wave number
L_{pile}	pile embedded length
R_T	rotor radius
t_c	concrete thickness of CFDST
t_{inner}	wall thickness of the inner steel tube of the innovative monopile
t_{outer}	wall thickness of the outer steel tube of the innovative monopile
$U_{current}$	local current velocity

UHPC	Ultra-high performance concrete
V_{hub}	wind speed at the hub height
V_z	wind profile
w_w	wave frequency
$\dot{x}$	wave induced velocity of water
$\ddot{x}$	wave induced acceleration of water
z	height above the sea water level
z_2	depth below sea surface
α	power law exponent
β	ratio of pile embedded length between the new and conventional monopile
λ	ratio of outer diameter between the new and conventional monopile
ρ	mass density of the sea water
ρ_a	air density
σ	concrete stress
ε	concrete strain
θ_N	pile accumulated rotation at mudline
θ_1	rotation obtained in the first loading cycle
ζ_{SDM}	cyclic increase factor
$\gamma^{'}$	soil effective unit weight
ξ	confinement factor
$\eta(t)$	surface wave profile
MSL	mean sea level
SLS	serviceability limit state
ULS	ultimate limit state

References

ABAQUS. User's Manual, Version 6.13. Karlsson & Sorenson, Inc., Pawtucket, Rhode Island.

ABS, 2010. Guide for Building and Classing Offshore Wind Turbine Installations. American Bureau of Shipping, ABS Plaza, USA.

Achmus, M., Kuo, Y.S., Abdel-Rahman, K., 2009. Behavior of monopile foundation under cyclic lateral load. Comput. Geotech. 36, 725–735.

Álamo, G.M., Aznárez, J.J., Padrón, L.A., Martínez-Castro, A.E., Gallego, R., Maeso, O., 2018. Dynamic soil-structure interaction in offshore wind turbines on monopiles in layered seabed based on real data. Ocean Eng. 156, 14–24.

Andres, A.D., MacGillivray, A., Roberts, O., Guanche, R., Jeffrey, H., 2017. Beyond LCOE: a study of ocean energy technology development and deployment attractiveness. Sustain. Energy Technol. Assess. 19, 1–16.

Arany, L., Bhattacharya, S., Macdonald, J., Hogan, J., 2017. Design of monopoles for offshore wind turbines in 10 steps. Soil Dyn. Earthq. Eng. 92, 126–152.

Barari, A., Bagheri, M., Rouainia, M., Ibsen, L.B., 2017. Deformation mechanisms for offshore monopile foundations accounting for cyclic mobility effects. Soil Dyn. Earthq. Eng. 97, 439–453.

Bocher, M., Mehmanparast, A., Braithwait, J., Shafiee, M., 2018. New shape function solutions for fracture mechanics analysis of offshore wind turbine monopile foundations. Ocean Eng. 160, 264–275.

CCES, 2018. Technical specification for concrete-filled double skin steel tubular structures. http://www.doc88.com/p-0009122357132.html. China.

Chen, S.M., Zhang, R., Jia, L.J., Wang, J.Y., Gu, P., 2018. Structural behavior of UHPC filled steel tube columns under axial loading. Thin-Walled Struct. 130, 550–563.

Christopher, D.J., Mohamed, A.M., Keri, L.R., 2017. Cost and Ecological Feasibility of Using UHPC in Highway Bridge, NDOT Research Report No. 224-14-803. Nevada Department of Transportation.

DNV·GL, 2016. DNVGL-ST-0437: Loads and Site Conditions for Wind Turbines. Det Norske Veritas, Oslo, Norway.

Eom, S.S., Vu, Q.V., Choi, J.H., Park, H.H., Kim, S.E., 2019. Flexural behavior of concrete-filled double skin steel tubes with a joint. J. Constr. Steel Res. 155, 260–271.

GB 500 17-2017, 2017. Code for Design of Steel Structure. China Architecture & Building Press, China.

Gentils, T., Wang, L., Kolios, A., 2017. Integrated structural optimisation of offshore wind turbine support structures based on finite element analysis and genetic algorithm. Appl. Energy 199, 187–204.

Gjersøe, N.F., Pedersen, E.B., Kristiansen, B., Hansen, N.E.O., Ibsen, L.B., 2015. Weight optimisation of steel monopile foundations for offshore windfarms. In: Proceedings of the Twenty-Fifth International Ocean and Polar Engineering Conference Kona. Big Island, USA.

GWEC, 2017. Global wind report: annual market update 2017. Global Wind Energy Council report.

Han, L.H., 2016. Concrete Filled Steel Tubular Structures: Theory and Practice, third ed. Science Press, Beijing.

Han, L.H., Li, Y.J., Liao, F.Y., 2011. Concrete-filled double skin steel tubular (CFDST) columns subjected to long-term sustained loading. Thin-Walled Struct. 49, 1534–1543.

Hassanein, M.F., Elchalakani, M., Karrech, A., Patel, V.I., Daher, E., 2018. Finite element modelling of concrete-filled double skin short compression members with CHS outer and SHS inner tubes. Mar. Struct. 61, 85–99.

Hermans, K.W., Peeringa, J.M., 2016. Future XL Monopile Foundation Design for a 10 MW Wind Turbine in Deep Water. ECN-E-16-069.

Hokmabadi, A.S., Fakher, A., Fatahi, B., 2012. Full scale lateral behaviour of monopile in granular marine soils. Mar. Struct. 29, 198–210.

Huang, H., 2005. Behavior of Concrete Filled Double-Skin Steel Tubular Beam-Columns, PhD Thesis. Fuzhou University, China.

Jammes, F.X., Cespedes, X., Resplendino, J., 2013. Design of Offshore Wind Turbines with UHPC, Symposium on Ultra-high Performance Fibre-Reinforced Concrete. Marseille, France.

Johnson, K., Karunasena, W., Sivakugan, N., Guazzo, A., 2001. Modeling pile-soil interaction using contact surfaces. Comput. Mech.-N. Front. New Millenn. 375–380.

Jonkman, J., Butterfield, S., Musial, W., Scott, G., 2009. Definition of a 5-MW Reference Wind Turbine for Offshore System Development. Technical Report NREL/TP-500-38060.

Kallehave, D., Byrne, B.W., Thilsted, C.L., Mikkelsen, K.K., 2015. Optimization of monopiles for offshore wind turbines. Philos. Trans. 373, 1–15.

Kim, H.G., Kim, B.J., 2018. Feasibility study of new hybrid piled concrete foundation for offshore wind turbine. Appl. Ocean Res. 76, 11–12.

Krahl, P.A., Carrazedo, R., Debs, M.K.E., 2018. Mechanical damage evolution in UHPFRC: experimental and numerical investigation. Eng. Struct. 170, 63–77.

Kuo, Y.S., 2008. On the Behavior of Large Diameter Piles under Cyclic Lateral Load. Ph. D Thesis. Leibniz University, Hannover, Germany.

Li, M.H., Zong, Z.H., Liu, L., Lou, F., 2018. Experimental and numerical study on damage mechanism of CFDST bridge columns subjected to contact explosion. Eng. Struct. 159, 265–276.

Li, W., Wang, T., Han, L.H., 2019. Seismic performance of concrete-filled double-skin steel tubes after exposure to fire: Experiments. J. Constr. Steel Res. 154, 209–223.

Liang, W., Dong, J.F., Wang, Q.Y., 2019. Mechanical behaviour of concrete-filled double-skin steel tube (CFDST) with stiffness under axial and eccentric loading. Thin-Walled Struct. 138, 215–230.

Ma, H.W., Yang, J., Chen, L.Z., 2017. Numerical analysis of the long-term performance of offshore wind turbines supported by monopiles. Ocean Eng. 136, 94–105.

Maryruth, B.P., 2014. XXL Monopile & Vibro-Hammers for Cheaper Offshore Wind. IQPC GmbH, Germany.

MIIC, 2018. Analysis of the Price Trend of World Steel Market, 2018, 5. Metallurgical industry information center, p. 55.

Mirzazadeh, M.M., Green, M.F., 2017. Non-linear finite element analysis of reinforced concrete beams with temperature differentials. Eng. Struct. 152 (1), 920–933.

Morató, A., Sriramula, S., Krishnan, N., Nichols, J., 2017. Ultimate loads and response analysis of a monopile supported offshore wind turbine using fully coupled simulation. Renew. Energy 101, 126–143.

Murphy, G., Igoe, D., Doherty, P., Gavin, K., 2018. 3D FEM approach for laterally loaded monopile design. Comput. Geotech. 100, 76–83.

Muskulus, M., Schafhirt, S., 2014. Design optimization of wind turbine support structures- A review. J. Ocean Wind Energy 1 (1), 12–22.

Negro, V., López-Gutiérrez, J., Esteban, M.D., Alberdi, P., Imaz, M., Serraclara, J.M., 2017. Monopiles in offshore wind: preliminary estimate of main dimensions. Ocean Eng. 133, 253–261.

Nie, W., Liu, Q.Y., 2002. Dynamic Analysis of Offshore Structures. Harbin Engineering University Press, Harbin, China.
NPCA, 2015. Guide to manufacturing architectural precast UHPC elements. https://precast.org/wp-content/uploads/2015/02/UHPC-White-Paper.pdf.
Ou, L., Xu, W., Yue, Q., Ma, C.L., Teng, X., Dong, Y.E., 2018. Offshore wind zoning in China: method and experience. Ocean Coast Manag. 151, 99–108.
O'Kelly, B.C., Arshad, M., 2016. Offshore Wind Turbine Foundations- Analysis and Design. Offshore Wind Farms Technologies, Design and Operation, pp. 589–610.
Rad, H., Turaj, A., Paul, L.C., Molenaar, D.P., 2014. Integrated multidisciplinary constrained optimization of offshore support structures. J. Phys. Conf. Ser. 555 (1), 1–10.
REN21, 2017. Renewables 2017 Global Status Report. Paris, France.
Scharff, R., Siems, M., 2013. Monopile foundations for offshore wind turbines – solutions for greater water depths. Steel Constr. 6 (1), 47–53.
Schmoor, K.A., Achmus, M., 2015. Optimum geometry of monopiles with respect to the geotechnical design. J. Ocean Wind Energy 2 (1), 54–60.
Schwanitz, V.J., Wierling, A., 2016. Offshore wind investments – realism about cost developments is necessary. Energy 106, 170–181.
Senanayake, A.I.M.J., 2016. Design of Large Diameter Monopiles for Offshore Wind Turbines in Clay. PhD Thesis. University of Texas at Austin.
Shafieifar, M., Farzad, M., Azizinamini, A., 2017. Experimental and numerical study on mechanical properties of Ultra High performance concrete (UHPC). Constr. Build. Mater. 156, 402–411.
Sheng, D., Eigenbrod, K.D., Wriggers, P., 2005. Finite element analysis of pile installation using large-slip frictional contact. Comput. Geotech. 32, 17–26.
Shimizu, M., Tatsumi, F., Ishikawa, T., Hattori, A., Kawano, H., 2013. Experimental study on ultimate strength of concrete filled double tubular steel with shear connector. Int. J. Steel Struct. 13 (1), 49–54.
Shirzadeh, R., Deveriendt, C., Bidakhvidi, M.A., Guillaume, P., 2013. Experimental and computational damping estimation of an offshore wind turbine on a monopile foundation. J. Wind Eng. Ind. Aerodyn. 120, 96–106.
Stansby, P.K., Devaney, L.C., Stallard, T.J., 2013. Breaking wave loads on monopiles for offshore wind turbines and estimation of extreme overturning moment. IET Renew. Power Gener. 7 (5), 514–520.
Strömblad, N., 2014. Modeling of Soil and Structure Interaction Subsea. Master's Thesis. Chalmers University of Technology, Sweden.
Thang, V., Marshall, P., Brake, N.A., Adam, F., 2016. Studded bond enhancement for steel-concrete-steel sandwich shells. Ocean Eng. 124, 32–41.
Uenaka, K., 2016. CFDST stub columns having outer circular and inner square sections under compression. J. Constr. Steel Res. 120, 1–7.
UHPC, 2017. Ultra high performance concrete made of NANODUR® Compound 5941. http://www.dyckerhoff.com/online/download.jsp?idDocument=315&instance=1.
Velarde, J., 2016. Design of Monopile Foundations to Support the DTU 10 MW Offshore Wind Turbine. Master's Thesis. Norwegian University of Science and Technology.
Wang, R., Han, L.H., Zhao, X.L., Rasmussen, K.J.R., 2016. Analytical behavior of concrete filled double steel tubular (CFDST) members under lateral impact. Thin-Walled Struct. 101, 129–140.
Wang, F.C., Han, L.H., Li, W., 2018. Analytical behavior of CFDST stub columns with external stainless steel tubes under axial compression. Thin-Walled Struct. 127, 756–768.
Wang, W.Q., Wu, C.Q., Li, J., Liu, Z.X., Zhi, X.D., 2019. Lateral impact behavior of double-skin steel tubular (DST) members with ultra-high performance fiber-reinforced concrete (UHPFRC). Thin-Walled Struct. 144, 106351.
Xu, H.B., 2015. Research on the Performance of HRB 500 Bars Reinforced Prestressed Ultra-high Performance Concrete Beams. PhD Thesis. Beijing University of Technology, China.
Yan, J.B., Zhang, W., Liew, J.Y.R., Li, Z.X., 2016. Numerical studies on shear resistance of headed stud connectors in different concretes under Arctic low temperature. Mater. Des. 112, 184–196.
Ye, Y., Han, L.H., Guo, Z.X., 2017. Concrete-filled bimetallic tubes (CFBT) under axial compression: analytical behaviour. Thin-Walled Struct. 119, 839–850.
Zhang, F.R., 2017. Dynamic Analysis of Steel Confined Concrete Tubular Columns against Blast Loads. PhD Thesis. The University of Adelaide, Austria.